Modeling, Numerical Methods, and Simulation for Particle-Fluid Two-Phase Flow Problems

QIANG ZHANG* AND MENGPING ZHANG*
Department of Mathematics
University of Science and Technology of China
Hefei, Anhui 230026, P.R. China
<zhqiang><mpzhang>@ustc.edu.cn

GUODONG JIN† AND DAYOU LIU†
Institute of Mechanics, Chinese Academy of Sciences
Beijing 100080, P.R. China
gd_jin@263.net   dyliu@mail.imech.ac.cn

CHI-WANG SHU‡
Division of Applied Mathematics, Brown University
Providence, RI 02912, U.S.A.
shu@cfm.brown.edu

Abstract—In this paper, we study the issues of modeling, numerical methods, and simulation with comparison to experimental data for the particle-fluid two-phase flow problem involving a solid-liquid mixed medium. The physical situation being considered is a pulsed liquid fluidized bed. The mathematical model is based on the assumption of one-dimensional flows, incompressible in both particle and fluid phases, equal particle diameters, and the wall friction force on both phases being ignored. The model consists of a set of coupled differential equations describing the conservation of mass and momentum in both phases with coupling and interaction between the two phases. We demonstrate conditions under which the system is either mathematically well posed or ill posed. We consider the general model with additional physical viscosities and/or additional virtual mass forces, both of which stabilize the system. Two numerical methods, one of them is first-order accurate and the other fifth-order accurate, are used to solve the models. A change of variable technique effectively handles the changing domain and boundary conditions. The numerical methods are demonstrated to be stable and convergent through careful numerical experiments. Simulation results for realistic pulsed liquid fluidized bed are provided and compared with experimental data. © 2004 Elsevier Ltd. All rights reserved.

Keywords—Particle-fluid two-phase flow, Fluidized bed, Two-phase models, WENO scheme, Experiments.

Typeset by $\mathcal{A}_{\mathcal{M}}\mathcal{S}$-TEX

1. INTRODUCTION

In this paper, we study the issues of modeling, numerical methods, and simulation with comparison to experimental data for the particle-fluid two-phase flow problem involving a solid-liquid mixed medium. The physical situation being considered is a pulsed liquid fluidized bed. The mathematical model is based on the assumption of one-dimensional flows, incompressible in both particle and fluid phases, equal particle diameters, and the wall friction force on both phases being ignored. The model consists of a set of coupled differential equations describing the conservation of mass and momentum in both phases with coupling and interaction between the two phases. We demonstrate conditions under which the system is either mathematically well posed or ill posed. We consider the general model with additional physical viscosities and/or additional virtual mass forces, both of which stabilizes the system. Two numerical methods, one of them is first-order accurate and the other fifth-order accurate, are used to solve the models. A change of variable technique effectively handles the changing domain and boundary conditions. The numerical methods are demonstrated to be stable and convergent through careful numerical experiments. Simulation results for realistic pulsed liquid fluidized bed are provided and compared with experimental data.

The equations we are solving in this paper are in the form of conservation laws

$$\frac{\partial u}{\partial t} + \frac{\partial f(u)}{\partial x} = G \tag{1.1}$$

or, in general, a first-order system

$$\frac{\partial u}{\partial t} + A(u)\frac{\partial u}{\partial x} = G, \tag{1.2}$$

where G contains forcing and possibly viscosity terms. Notice that (1.1) is a special case of (1.2) with $A(u) = \frac{\partial f(u)}{\partial u}$. System (1.2) is called hyperbolic (when G does not contain viscosity terms) if the eigenvalues of the matrix $A(u)$ are all real and there is a complete set of independent eigenvectors. Hyperbolic systems are mathematically well posed, meaning that their solutions depend continuously on the initial conditions. This can be proven for the linear case and also for some nonlinear cases. On the other hand, if the eigenvalues of $A(u)$ have nonzero imaginary parts, the system becomes elliptic. Typically, the system becomes elliptic only in certain regions of u and remains hyperbolic in other regions. Such systems are called mixed type. Elliptic and mixed-type systems are *not* mathematically well posed. Perturbations in high modes grow in an unbounded way. Such systems are very difficult to simulate numerically.

In recent years, many high-order, high-resolution numerical methods have been developed in the literature to solve hyperbolic systems. The main applications are in computational fluid dynamics, but there are also applications in other physical and engineering areas. In this paper, we apply both low-order and high-order finite-difference WENO (weighted essentially nonoscillatory) schemes [1,2] to solve both the well-posed and ill-posed models. In particular, fifth-order WENO schemes in [1] and splitting techniques in [3] to treat mixed-type systems are used. The numerical procedures are summarized in Section 3. These numerical methods are found to be very useful in computational fluid dynamics and in other applications, because of their simultaneous high-order accuracy and nonoscillatory property in the presence of shocks and other discontinuities or sharp gradient regions in the solution, or in general for convection dominated problems. For a review of such methods, see [4].

The simulation and experiments reported in this paper are for the fluidized beds. Fluidized beds are common and important reactors in process engineering such as catalytic reactions and bioreactions because of the high contact efficiency between the fluid and solid. It is well known that there are concentration nonuniform structures such as bubbles and slugs in fluidization. Bubbling and slugging are undesirable for efficient operations, because they can reduce the contact efficiency. Lots of studies show that fluidization quality can be significantly improved by

externally applied vibrations or pulses, e.g., [5–7]. However, the theoretical understanding of pulsed fluidized beds is far from complete.

It is well known that the widely used two-fluid model, referred as the basic equation set in [8] or Model A in [9] without the particle stress, is ill posed and was discussed by Gidaspow [10] and in more detail by Lyczkowski [11]. A well-posed model was given first by Rudinger and Chang [12] and was extended by Lyczkowski [11] and is referred as Model B in [9]. The two models have the same mixture momentum equations. The major difference between the two models is that, in the latter one, all pressure drops are in the continuous phase momentum equations, without any pressure drop in the solid phase momentum equation.

Drew *et al.* [13] proposed a generalized formulation of added mass force. The model is objective, that is, frame indifferent. Lahey, Jr. *et al.* [14] studied the effect of the added mass on numerical stability and computation efficiency on steady bubbles/liquid flow through nozzles and diffusers using Model A with the above added mass force formulation. Their investigations have shown that the inclusion of appropriate virtual mass effects into the two-fluid model does not appreciably change the numerical results but is a physically realistic way to improve numerical stability and computation efficiency and to achieve accurate results.

Jones and Prosperetti [15] examined the suitability of the general class of Model A, that is, the first-order differential models for two-phase flow problems. They carried out an analysis of the linear stability of steady uniform flow in a straight pipe and derived two explicit stability criteria against small perturbations. They illustrated their theory using three specific models, one of them is the model with the added mass formulation of Drew *et al.* [13]. A review on the modeling of disperse multiphase flows has been given by Prosperetti [16]. A general result on the relationship between the hyperbolicity and stability was presented and its implications were discussed.

The organization of the paper is as follows. In Section 2, we present the mathematical models of the two-phase flow under consideration. We emphasize two features in the general model to stabilize the system. One is the additional physical viscosities, and the other is the additional virtual mass force parameterized by the virtual volume coefficient C and a free parameter λ, the details of which will be provided in Section 2. The additional physical viscosities render the system to be incomplete parabolic; and the additional virtual mass force renders the system hyperbolic under certain combinations of C and λ. In Section 3, we present two numerical methods to be used for the simulations in this paper. The first method is a first-order Lax-Friedrichs-type scheme, which is adapted as in [3] to effectively simulate both hyperbolic and mixed-type systems. The second one is a fifth-order WENO-type method [1], suitable for simulating hyperbolic or incomplete parabolic systems. In Section 4, we describe our experimental apparatus and method. Section 5 contains our simulation results and comparisons with experimental data. Concluding remarks are provided in Section 6.

2. MODELS OF THE TWO-PHASE FLOW

The continuity and momentum equations for the solid phase and the fluid phase are, respectively, (e.g., [17])

$$\frac{\partial}{\partial t}\left(\alpha_p \rho_p\right) + \frac{\partial}{\partial x}\left(\alpha_p \rho_p u_p\right) = 0,$$

$$\frac{\partial}{\partial t}\left(\alpha_f \rho_f\right) + \frac{\partial}{\partial x}\left(\alpha_f \rho_f u_f\right) = 0,$$

$$\frac{\partial}{\partial t}\left(\alpha_p \rho_p u_p\right) + \frac{\partial}{\partial x}\left(\alpha_p \rho_p u_p^2\right) + \alpha_p \frac{\partial P}{\partial x} = -\alpha_p \rho_p g + F_p + \varepsilon_1 \frac{\partial^2}{\partial x^2}\left(\alpha_p \rho_p u_p\right), \qquad (2.1)$$

$$\frac{\partial}{\partial t}\left(\alpha_f \rho_f u_f\right) + \frac{\partial}{\partial x}\left(\alpha_f \rho_f u_f^2\right) + \alpha_f \frac{\partial P}{\partial x} = -\alpha_f \rho_f g - F_p + \varepsilon_2 \frac{\partial^2}{\partial x^2}\left(\alpha_f \rho_f u_f\right),$$

$$\alpha_p + \alpha_f = 1,$$

$$\alpha_p u_p + \alpha_f u_f = U\left(t\right).$$

Here, α_p and α_f are the volume fractions of particles and fluids, respectively, in the mixture. u_p and u_f are the velocities, and ρ_p and ρ_f are the (constant) densities of particles and fluids, respectively. P is the pressure, g is the gravity acceleration, $U(t)$ is a given function of t, measuring the instantaneous fluid inlet rate (or fluidization velocity), controlled by a time-lag relay and electromagnetic valve in our experiment. F_p is the interaction force per unit volume between the solid and fluid phases, given by $F_p = F_o + F_c$, where F_o represents a drag force being a function of the local relative velocity $(u_f - u_p)$ and is often expressed as ([18,19])

$$F_o = \frac{\rho_p - \rho_f}{u_T} g \alpha_p \alpha_f^{1-n} \left(u_f - u_p \right), \tag{2.2}$$

where, for uniform sized particles, the index n depends on the particle Reynolds number, $\mathrm{Re}_p = u_T d_p \rho_f / \mu_f$ with d_p denoting the diameter of the particles and μ_f denoting the viscosity coefficient of the fluid, n decreases with an increase of Re_p, reaching $n = 1.39$ when $\mathrm{Re}_p > 500$, see [20]. u_T is the terminal velocity of a single particle in a static fluid (when the drag force of the fluid acting on the particle balances with the weight of the particle in the fluid) and can be calculated as

$$u_T = \frac{d_p^2 \left(\rho_p - \rho_f \right)}{k \mu_f} g.$$

For nonuniform sized particles, the expression above is just for a reference. F_c represents the virtual (or added) mass force related to the local relative acceleration. A good expression for this force has not been well researched yet. The following expression was given by Drew *et al.* [13]

$$F_c = -C \alpha_p \rho_f \left[\frac{\partial u_p}{\partial t} + u_f \frac{\partial u_p}{\partial x} - \frac{\partial u_f}{\partial t} - u_p \frac{\partial u_f}{\partial x} - (1 - \lambda)(u_f - u_p) \frac{\partial (u_f - u_p)}{\partial x} \right]. \tag{2.3}$$

Here, C is the virtual volume coefficient and λ is a free parameter. Drew *et al.* [13] treated them as model parameters being functions of α_p. According to their opinion, the range of these parameters should be $0 < C < 0.5$ and $0 < \lambda < 2$, and when $\alpha_p \to 0$ (as the limiting case of a single particle moving in an infinite flow field), then $C = 0.5$ (this can be proved by the theory of fluid mechanics) and $\lambda = 2$ (this is more heuristic).

The physical motivation for the additional physical viscosities in the momentum equations in (2.1) parameterized by ε_1 and ε_2 is the normal stresses τ_{pxx} and τ_{fxx}, whose x-derivatives are added to the two momentum equations. In a nonhomogeneous bed, the normal stress can be expressed as $\tau_{pxx} = \mu_p \frac{\partial u_p}{\partial x}$, where μ_p is the particle viscosity. No theory or experimental data about μ_p is available. Batchelor [21], Anderson *et al.* [22], and Glasser *et al.* [19,23] gave two different conjectures for μ_p. Clearly, ε_1 and ε_2 have similar meanings as those for μ_p and μ_f. We have taken them as constants in this paper for simplicity.

We use the dimensional form of the equation (2.1) with meter-kg-second measuring system. As we mentioned before in the introduction, this model is based on the assumption of one-dimensional flows, incompressible in both particle and fluid phases, equal particle diameters, and the wall friction force on both phases being ignored.

We remark that the last equation in (2.1) can be obtained from the first two continuity equations and the second last equation, and hence, is not an independent equation. Notice that there are only two independent evolution equations in (2.1), due to the last two constraints. We choose to write out the equations for α_p and u_p and eliminate all the other variables, resulting in the following *nonconservative* form of systems:

$$
\begin{aligned}
\frac{\partial \alpha_p}{\partial t} + A_1 \frac{\partial \alpha_p}{\partial x} + B_1 \frac{\partial u_p}{\partial x} &= 0, \\
\frac{\partial u_p}{\partial t} + A_2 \frac{\partial \alpha_p}{\partial x} + B_2 \frac{\partial u_p}{\partial x} &= D + E,
\end{aligned}
\tag{2.4}
$$

where

$$A_1 = u_p,$$

$$B_1 = \alpha_p,$$

$$A_2 = -\frac{\rho_r \left(u_f - u_p\right)^2 \left[\alpha_f + C\left(1 - \lambda\right)\right]}{\alpha_f \left(\alpha_f + \alpha_p \rho_r\right) + C\rho_r},$$

$$B_2 = \frac{\alpha_p \alpha_f \rho_r \left(2u_f - u_p\right) + \alpha_f^2 u_p + C\rho_r \left[2u_f - u_p - \lambda\left(u_f - u_p\right)\right]}{\alpha_f(\alpha_f + \alpha_p \rho_r) + C\rho_r},$$

$$D = -g + \frac{\rho_r \left(g + U'\left(t\right)\right)\left(\alpha_f + C\right)}{\alpha_f \left(\alpha_f + \alpha_p \rho_r\right) + C\rho_r} + \frac{\alpha_f^{2-n}\left(1 - \rho_r\right)g\left(u_f - u_p\right)}{\alpha_f\left(\alpha_f + \alpha_p \rho_r\right) + C\rho_r} \cdot \frac{1}{u_T}.$$

(2.5)

If we using the model with $C > 0$, then we set $\varepsilon_1 = \varepsilon_2 = 0$; otherwise, we need the viscosity terms to make the system well posed, thus,

$$E = \frac{\varepsilon_1 \alpha_f + \varepsilon_2 \alpha_p \rho_r}{\alpha_p \left(\alpha_f + \alpha_p \rho_r\right)} \frac{\partial^2}{\partial x^2}\left(\alpha_p u_p\right).$$

Here, $\rho_r = \rho_f / \rho_p$. Notice that it is impossible to write the momentum equation in conservation form if we eliminate the pressure P. We thus have adopted this nonconservative form for the simulation. This is allowed as long as no shocks or other discontinuities appear.

To check if system (2.4) is mathematically well posed (when the viscosity term $E = 0$), we look at the eigenvalues of the Jacobian

$$\begin{pmatrix} A_1 & B_1 \\ A_2 & B_2 \end{pmatrix},$$

which are given by

$$\nu_{1,2} = \frac{Q}{2R} \pm \frac{\Delta u}{R}\left(\frac{\rho_r}{\alpha_f \alpha_p}\right)^{1/2} H^{1/2},$$

where $\Delta u = u_f - u_p$, and

$$R = \frac{\rho_r}{\alpha_f} + \frac{1}{\alpha_p} + \frac{\rho_r}{\alpha_f^2 \alpha_p}C,$$

$$Q = \frac{2\rho_r u_f}{\alpha_f} + \frac{2u_p}{\alpha_p} + \frac{C\rho_r}{\alpha_f^2 \alpha_p}\left[u_f + u_p + \left(1 - \lambda\right)\Delta u\right],$$

$$H = -1 + \frac{C}{\alpha_f}\left(1 - \lambda\right)\left(\rho_r - 1\right) + \frac{1}{4}\frac{\rho_r}{\alpha_f \alpha_p}\left(\frac{C}{\alpha_f}\right)^2\left\{1 + 2\left(\alpha_f - \alpha_p\right)\left(1 - \lambda\right) + \left(1 - \lambda\right)^2\right\}.$$

Notice that these eigenvalues are real only if $H \geq 0$. This, for example, is never true when $C = 0$. Thus, the system without physical viscosity is always ill posed if no additional virtual mass force characterized by C and λ is added.

We remark that preliminary simulation results using a Lax-Wendroff-type scheme were provided in [24], for the model with $C = 0$, with also comparison with experimental results. The study in this paper is however more exhaustive both in the generality of the models (including those with $C > 0$ and the physical viscosities) and in the accuracy and robustness of the numerical methods. Moreover, the experimental results for both the bed height $h(t)$ and the particle concentration α_p are obtained in data form and compared with the simulation results.

3. NUMERICAL METHODS

In the simulation presented in Section 5, the computational domain is given by $0 \leq x \leq h(t)$, with an initial value given as

$$
\begin{aligned}
\alpha_p(x,0) &= 1 - \left(\frac{U(0)}{u_T} \right)^{1/(n+1)}, \\
u_p(x,0) &= 0, \\
u_f(x,0) &= \frac{U(0)}{1 - \alpha_p(x,0)}, \\
h(0) &= h_0.
\end{aligned}
\tag{3.1}
$$

The boundary condition is given by

$$
\begin{aligned}
x = 0 : u_p(0,t) = 0, \qquad \alpha_p(0,t) &= 1 - \left(\frac{U(t)}{u_T} \right)^{1/(n+1)}, \\
x = h(t) : \frac{dh(t)}{dt} &= u_p(h(t),t).
\end{aligned}
\tag{3.2}
$$

In the simulation, the length of the computational domain $[0, h(t)]$ is changing with the time t according to the boundary condition (3.2) which describes the evolution of the bed height $h(t)$ when the velocity u_p at the right (top) boundary is given. An efficient method for the computation is through a transformation

$$
x = \frac{h(t)}{h_0} \xi \qquad \text{and} \qquad t = \tau,
$$

where (x,t) is the original physical coordinate and (ξ, τ) is the computational coordinate in which the spatial mesh size is kept uniform. If we define

$$
C_0 = \frac{h_0}{h(t)}, \qquad C_1 = \frac{h'(t)}{h(t)} = \frac{u_p(h(t),t)}{h(t)},
$$

then we have

$$
\frac{\partial}{\partial t} = \frac{\partial}{\partial \tau} - C_1 \xi \frac{\partial}{\partial \xi}, \qquad \frac{\partial}{\partial x} = C_0 \frac{\partial}{\partial \xi},
$$

and the eigenvalues of the Jacobian in the new coordinate system (ξ, τ) are given by

$$
\hat{\nu}_{1,2} = C_0 \nu_{1,2} - C_1 \xi.
\tag{3.3}
$$

The final system to be solved numerically is thus

$$
\begin{aligned}
\frac{\partial \alpha_p}{\partial \tau} + \tilde{A}_1 \frac{\partial \alpha_p}{\partial \xi} + \tilde{B}_1 \frac{\partial u_p}{\partial \xi} &= 0, \\
\frac{\partial u_p}{\partial \tau} + \tilde{A}_2 \frac{\partial \alpha_p}{\partial \xi} + \tilde{B}_2 \frac{\partial u_p}{\partial \xi} &= D,
\end{aligned}
\tag{3.4}
$$

where

$$
\begin{aligned}
\tilde{A}_1 &= C_0 u_p - C_1 \xi, \\
\tilde{B}_1 &= C_0 \alpha_p, \\
\tilde{A}_2 &= -\frac{C_0 \rho_r (u_f - u_p)^2 [\alpha_f + C(1-\lambda)]}{\alpha_f (\alpha_f + \alpha_p \rho_r) + C \rho_r}, \\
\tilde{B}_2 &= \frac{C_0 \left\{ \alpha_p \alpha_f \rho_r (2u_f - u_p) + \alpha_f^2 u_p + C \rho_r [2u_f - u_p - \lambda (u_f - u_p)] \right\}}{\alpha_f (\alpha_f + \alpha_p \rho_r) + C \rho_r} - C_1 \xi,
\end{aligned}
$$

for the case $C > 0$, where D is still given by (2.5), and

$$\frac{\partial \alpha_p}{\partial \tau} + \frac{\partial (C_0 \alpha_p u_p - C_1 \xi \alpha_p)}{\partial \xi} = -C_1 \alpha_p,$$

$$\frac{\partial u_p}{\partial \tau} - \frac{C_0 \rho_r}{\alpha_f + \rho_r \alpha_p} \frac{\partial \left(\alpha_p u_p^2 + \alpha_f u_f^2 \right)}{\partial \xi} + \frac{\partial ((C_0/2) u_p^2 - C_1 \xi u_p)}{\partial \xi} = -C_1 u_p + \tilde{E} + F,$$

(3.5)

where

$$F = (\alpha_f + \rho_r \alpha_p)^{-1} \left\{ \rho_r U'(t) + (\rho_r - 1) \alpha_f g \left[1 - \frac{\alpha_f^{-n} (u_f - u_p)}{u_T} \right] \right\}$$

and

$$\tilde{E} = \frac{C_0^2 (\varepsilon_1 \alpha_f + \varepsilon_2 \alpha_p \rho_r)}{\alpha_p (\alpha_f + \alpha_p \rho_r)} \frac{\partial^2}{\partial \xi^2} (\alpha_p u_p),$$

for the case $C = 0$. Notice that, for the simpler case (3.5), we have written the system grouping as many terms in a conservation form as possible.

We now describe the numerical methods used in solving systems (3.4) and (3.5). We first describe spatial discretizations. Two different numerical methods are used.

The first method is a simple first-order accurate Lax-Friedrichs-type spatial discretization, adjusted as in [3] to handle mixed-type systems. Thus, all the first derivative terms in (3.4) and (3.5) are approximated by a second-order central difference formula. For example, $\frac{\partial \alpha_p}{\partial \xi}$ in the second equation of (3.4) is discretized by the formula

$$\left. \frac{\partial \alpha_p}{\partial \xi} \right|_{\xi = \xi_j} \approx \frac{(\alpha_p)_{j+1} - (\alpha_p)_{j-1}}{2 \Delta \xi}.$$

To correct the instability caused by central approximations, we add numerical viscosity terms to the equations in (3.4) and (3.5). To the first equation in (3.4) and (3.5), we add a term

$$\frac{C_0 \beta_1 \sigma}{\Delta \xi} \left((\alpha_p)_{j+1} - 2 (\alpha_p)_j + (\alpha_p)_{j-1} \right),$$

(3.6)

and to the second equation in (3.4) and (3.5), we add a term

$$\frac{C_0 \beta_2 \sigma}{\Delta \xi} \left((u_p)_{j+1} - 2 (u_p)_j + (u_p)_{j-1} \right),$$

(3.7)

where σ is the maximum in absolute value of the eigenvalues defined in (3.3) taken over the whole ξ line. β_1 and β_2 are two constants, which can actually change with the mesh size $\Delta \xi$: as long as they do not grow as fast as $1/\Delta \xi$, the terms defined above will approach zero when $\Delta \xi \to 0$, and hence, can be justified as numerical (rather than physical) viscosities. We take $\beta_2 = 0$ for the second equation in (3.5), since the physical viscosities already take effect in this equation.

The second method is the high-order weighted essentially nonoscillatory (WENO) method. In particular, we use the fifth-order WENO finite-difference method in [1]. The advantage of the WENO scheme is that it maintains uniform high-order accuracy while automatically adapting its reliance on local stencils to obtain information from a locally smoothest region, hence, avoiding numerical oscillations and instabilities when the solution contains either shocks or sharp gradient regions. The higher-order accuracy of the method allows us to use fewer grid points to obtain good resolution of the solution. Thus, for any of the first derivative terms, such as $\frac{\partial g}{\partial \xi}$ with $g = \alpha_p$, we discretize it by a fifth-order conservative WENO difference formula

$$\left. \frac{\partial g}{\partial \xi} \right|_{\xi = \xi_j} \approx \frac{1}{\Delta \xi} \left(\hat{g}_{j+1/2} - \hat{g}_{j-1/2} \right),$$

where the numerical flux $\hat{g}_{j+1/2}$ is obtained with the following procedure. We describe only the construction of this numerical flux with a left-biased stencil, suitable for computing the derivative with a positive flow direction. The procedure for the numerical flux with a right-biased stencil would just be a mirror symmetry with respect to $j+1/2$ when computing $\hat{g}_{j+1/2}$. We obtain the numerical flux by

$$\hat{g}_{j+1/2} = \omega_1 \hat{g}^{(1)}_{j+1/2} + \omega_2 \hat{g}^{(2)}_{j+1/2} + \omega_3 \hat{g}^{(3)}_{j+1/2},$$

where $\hat{g}^{(m)}_{j+1/2}$ are three third-order fluxes on three different stencils given by

$$\hat{g}^{(1)}_{j+1/2} = \frac{1}{3} g_{j-2} - \frac{7}{6} g_{j-1} + \frac{11}{6} g_j,$$

$$\hat{g}^{(2)}_{j+1/2} = -\frac{1}{6} g_{j-1} + \frac{5}{6} g_j + \frac{1}{3} g_{j+1},$$

$$\hat{g}^{(3)}_{j+1/2} = \frac{1}{3} g_j + \frac{5}{6} g_{j+1} - \frac{1}{6} g_{j+2},$$

and the nonlinear weights ω_m are given by

$$\omega_m = \frac{\tilde{\omega}_m}{\sum\limits_{l=1}^{3} \tilde{\omega}_l}, \qquad \tilde{\omega}_l = \frac{\gamma_l}{(\varepsilon + s_l)^2},$$

with the linear weights γ_l given by

$$\gamma_1 = \frac{1}{10}, \qquad \gamma_2 = \frac{3}{5}, \qquad \gamma_3 = \frac{3}{10},$$

and the smoothness indicators s_l given by

$$s_1 = \frac{13}{12} (g_{j-2} - 2g_{j-1} + g_j)^2 + \frac{1}{4} (g_{j-2} - g_{j-1} + 3g_j)^2,$$

$$s_2 = \frac{13}{12} (g_{j-1} - 2g_j + g_{j+1})^2 + \frac{1}{4} (g_{j-1} - g_{j+1})^2,$$

$$s_3 = \frac{13}{12} (g_j - 2g_{j+1} + g_{j+2})^2 + \frac{1}{4} (3g_j - 4g_{j+1} + g_{j+2})^2.$$

Finally, ε is a parameter to avoid the denominator to become 0 and is taken as $\varepsilon = 10^{-6}$ in the computation of this paper.

Thus, for the conservative terms, i.e., the terms $\frac{\partial (C_0 \alpha_p u_p - C_1 \xi \alpha_p)}{\partial \xi}$ and $\frac{\partial ((C_0/2) u_p^2 - C_1 \xi u_p)}{\partial \xi}$ in (3.5), we perform a Lax-Friedrichs flux splitting

$$f^+ = \frac{1}{2} (f + \gamma \sigma \alpha_p), \qquad f^- = f - f^+, \tag{3.8}$$

for $f = (C_0 \alpha_p u_p - C_1 \xi \alpha_p)$, and

$$f^+ = \frac{1}{2} (f + \gamma \sigma u_p), \qquad f^- = f - f^+, \tag{3.9}$$

for $f = ((C_0/2) u_p^2 - C_1 \xi u_p)$, where σ is again the maximum in absolute value of the eigenvalues defined in (3.3) taken over the whole ξ line, and γ is a constant controlling the numerical viscosities in this flux splitting. γ can change with the mesh size $\Delta \xi$. As long as it does not grow as fast as $1/\Delta \xi$, the numerical viscosity will vanish together with $\Delta \xi$ and the scheme is still at least formally fourth-order accurate, justifying the scheme as a high-order method. The WENO flux difference approximation is then used, with a left-biased flux to approximate the derivative of f^+, and a

right-biased flux to approximate the derivative of f^-. The sum of them is then an approximation to the derivative of f.

We now describe the WENO recipe for the nonconservative first derivative terms, such as all the first derivative terms in (3.4) and the term $-(C_0\rho_r/(\alpha_f + \rho_r\alpha_p))\frac{\partial(\alpha_p u_p^2 + \alpha_f u_f^2)}{\partial\xi}$ in (3.5). The approximation for the "diagonal terms", namely, $\tilde{A}_1\frac{\partial\alpha_p}{\partial\xi}$ in the first equation of (3.4) and $\tilde{B}_2\frac{\partial u_p}{\partial\xi}$ in the second equation of (3.4), is taken as an upwind-biased WENO approximation. Namely, if the coefficient, for example, $c_j = (\tilde{A}_1)_j$, is positive, then the derivative $\frac{\partial\alpha_p}{\partial\xi}$ is approximated by a left-biased stencil based WENO; otherwise, it is approximated by a right-biased stencil-based WENO. For all the other terms, the WENO approximation is central, namely, taken as the average of the the left-biased stencil based approximation and the right-biased stencil based approximation. Finally, the numerical viscosity terms in (3.6) and (3.7) are added. This seems necessary, not to control any instability, but to maintain the bed height $h(t)$ to reach a periodic (in time) pattern. See Section 5 for details.

We now describe the time discretization. For the first-order Lax-Friedrichs-type approximation, a simple Euler forward is used in time. For the fifth-order WENO scheme, we use the following third-order TVD Runge-Kutta time discretization [25]:

$$\phi^{(1)} = \phi^n + \Delta t L\left(\phi^n, t^n\right),$$
$$\phi^{(2)} = \frac{3}{4}\phi^n + \frac{1}{4}\phi^{(1)} + \frac{1}{4}\Delta t L\left(\phi^{(1)}, t^n + \Delta t\right),$$
$$\phi^{n+1} = \frac{1}{3}\phi^n + \frac{2}{3}\phi^{(2)} + \frac{2}{3}\Delta t L\left(\phi^{(2)}, t^n + \frac{1}{2}\Delta t\right),$$

where ϕ represents the quantities to be evolved in time, namely, α_p, u_p, and $h(t)$, and L is the approximation to the spatial derivatives and the forcing terms (the right-hand side of the ODE for the time variable t when all spatial derivatives have been discretized). Notice that this TVD Runge-Kutta method is just a convex combination of three simple Euler forward time discretizations.

We finally summarize the computational procedure as follows. We only describe the procedure for Euler forward in time, since the third-order TVD Runge-Kutta method is just a convex combination of three such Euler forward steps.

1. Given α_p, u_p and $h(t)$ at $t = t^n$, compute α_f and u_f at $t = t^n$ by the last two equations of (2.1).
2. Compute all the spatial derivatives and forcing terms in (3.4) or (3.5) using one of the numerical methods described above.
3. Update the bed height $h(t)$ by

$$h\left(t^{n+1}\right) = h\left(t^n\right) + \Delta t u_p\left(h\left(t^n\right), t^n\right).$$

4. Update α_p, u_p using Euler forward, and go back to Step 1.

4. EXPERIMENTAL APPARATUS AND METHOD

Figure 1 is the schematic diagram of the experimental apparatus. The experiments have been carried out under ambient conditions in a 29 ID and 1150 high perspex column fitted with a porous plate distributor. The variations of bed height and particle concentration have been recorded using a Sony® digital video camera recorder (DCR-TRV6E).

Particles are fluidized by pulsed liquid. The liquid flows through two routes: one is a steady flow and the other is a pulsed flow. The two routes intersect before liquid flows through a section with packed particles, then into the bed to make the flow uniform. The flux is measured using a stopwatch and a platform balance. The sketch map of flux vs. time is illustrated in Figure 2. The pulse frequency, and the time of on-period and off-period are controlled by the graded time-lag relay.
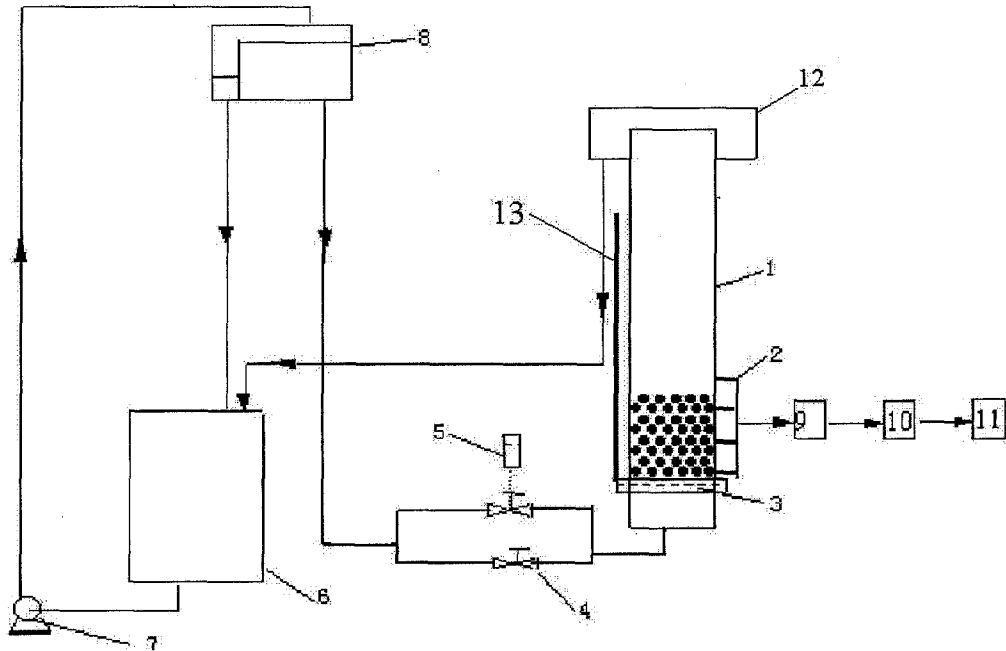
Figure 1. Schematic diagram of the experimental apparatus. 1: fluidized bed; 2: pressure transducer; 3: plate distributor; 4: spheric valve; 5: time-lag relay and electromagnetic valve; 6: lower water tank; 7: centrifugal pump; 8: upper water tank; 9: amplifier; 10: A/D converter; 11: computer; 12: water gathering vessel; 13: ruler.
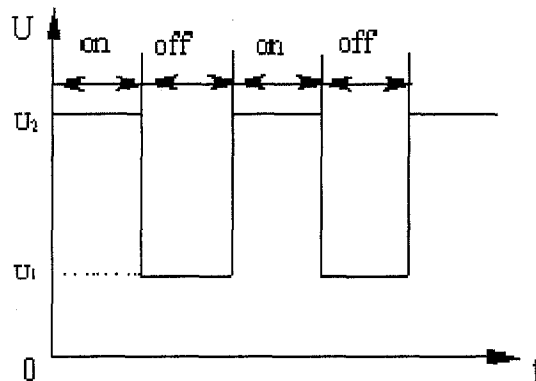

Figure 2. Illustration diagram of flow rate varying with time.

We now describe the experimental method. We put a ruler beside the bed in the experiment and record the variation process of the bed height by the camera. The camera can record 25 frames per second. The variation of bed height vs. time is measured from a frame by frame playing of the tape. In order to get the concentration distribution, we must calibrate the relation between the particle concentration and the scale of the photos. We carry out the experiment at night, and use six 500W iodine-tungsten lamps in vertical direction to get uniform background light. We make space corrections considering the nonuniform exposure of the film even to a uniform light. For example, Figure 3a shows that, even for a uniform state, throughout the bed, the scale of the photo is still nonuniform along the bed. After we make the corrections, we can get a much more uniform distribution of the particle concentration, and the standard deviation is about 0.7% and the system error is about 1.0%, Figure 3b. This is allowable for dense two-phase flow measurement in the overall flow field.
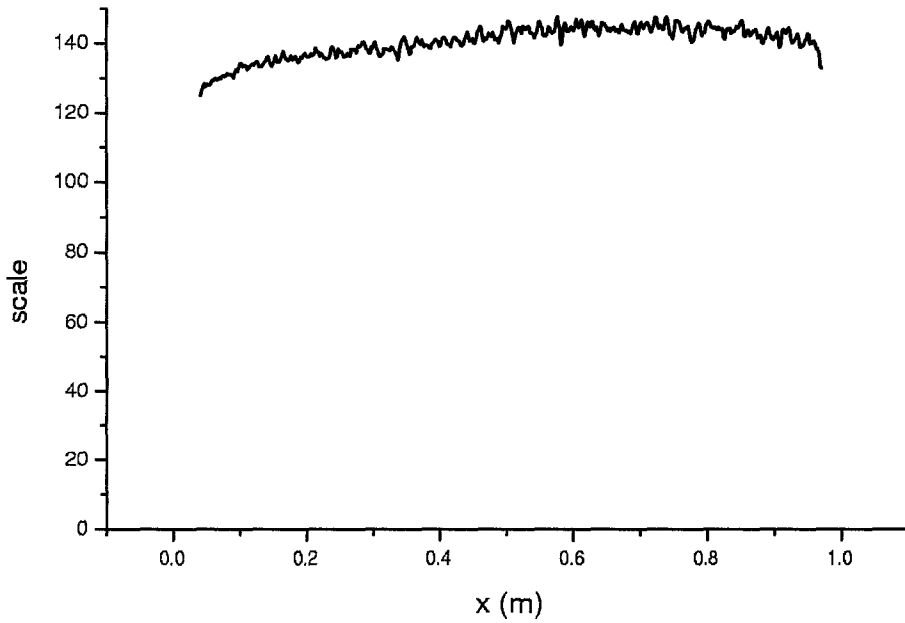
(a) Nonuniformity of the scale of the photo along the bed for uniform concentration.
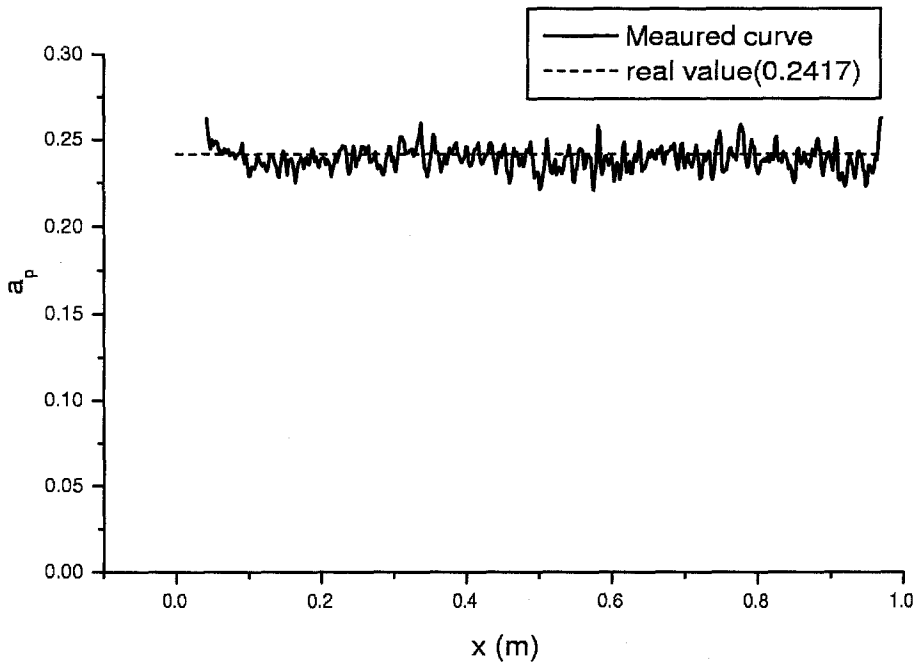
(b) Particle concentration after correction.

Figure 3.

5. SIMULATION RESULTS AND COMPARISON WITH EXPERIMENTS

In the numerical tests, we consider the initial and boundary conditions (3.1),(3.2) with

$$U\left(t\right) = \begin{cases} U_1, & C_{T,1} < t \leq C_{T,2}, \\ U_2, & 0 < t \leq C_{T,1}, \end{cases}$$

Table 1. Summary of the three test cases.

	U_2(m/s)	U_1(m/s)	$C_{T,1}$(s)	$C_{T,2}$(s)	n	U_T(m/s)	h_0(m)
Case 1	0.1020	0.0400	4	8	1.44	0.194	0.909
Case 2	0.1541	0.0376	2	6	1.44	0.194	0.476
Case 3	0.0550	0.1062	6	9	1.44	0.191	1.365

and periodically extended with period $C_{T,2}$. Note that $U(0) = U_1$ as initial condition. Three cases are studied in the numerical simulation: the corresponding parameters for these cases are given in Table 1.

Furthermore, we have $\rho_f = 1000\,\text{kg/m}^3$ and $\rho_p = 2500\,\text{kg/m}^3$.

In all the simulations, we set the CFL number to be 0.1, where the CFL number is defined by

$$\sigma \frac{\Delta t}{\Delta \xi} + \frac{C_0^2 \left(\varepsilon_1 \alpha_f + \varepsilon_2 \alpha_p \rho_r\right)}{\alpha_p \left(\alpha_f + \alpha_p \rho_r\right)} \frac{\Delta t}{\Delta \xi^2}$$

and σ is again the largest eigenvalue (in absolute value) of the Jacobian in (3.3) over the whole ξ line and ε_1 and ε_2 are the physical viscosity coefficients. For the model with $C = 0$, we set the coefficients of the physical viscosity as $\varepsilon_1 = \varepsilon_2 = 10^{-5}$. For the model with $C > 0$, we do not include any physical viscosity ($\varepsilon_1 = \varepsilon_2 = 0$) and set $C = 0.5$ and $\lambda = 3$ for all the test cases. Ideally, we would like to keep λ between 0 and 2, however, it seems that the system is still ill posed when λ is in this range. The choices for C and λ are taken after extensive numerical experiments to guarantee hyperbolicity and good numerical results.

Numerical simulations are continued for a long time until a steady periodic pattern is observed.

Figures 4–15 contain comparisons between the experimental data and the simulation results for the bed height $h(t)$, for the three cases and two numerical methods. The square symbols represent the experimental data, the circles represent the numerical simulation results with a coarser mesh, and the lines represent the numerical simulation results with a refined mesh. For the first-order method, we use 300 points for the coarser mesh and 600 points for the refined mesh; for the fifth-order WENO method, we use 150 points for the coarser mesh and 300 points for the refined mesh.
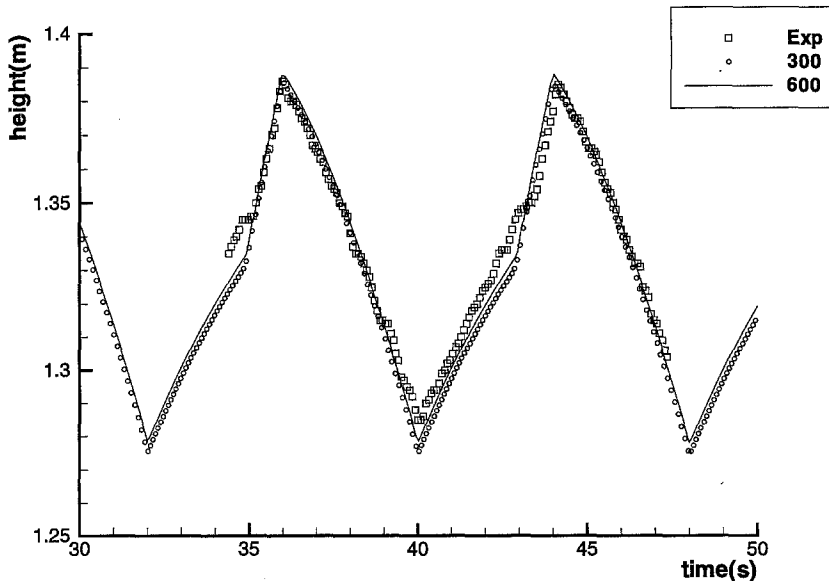
Figure 4. Case 1 with $C = 0$. First-order numerical method. Squares are the experimental data, circles are the simulation result with 300 grid points, and the solid line is the simulation result with 600 grid points.
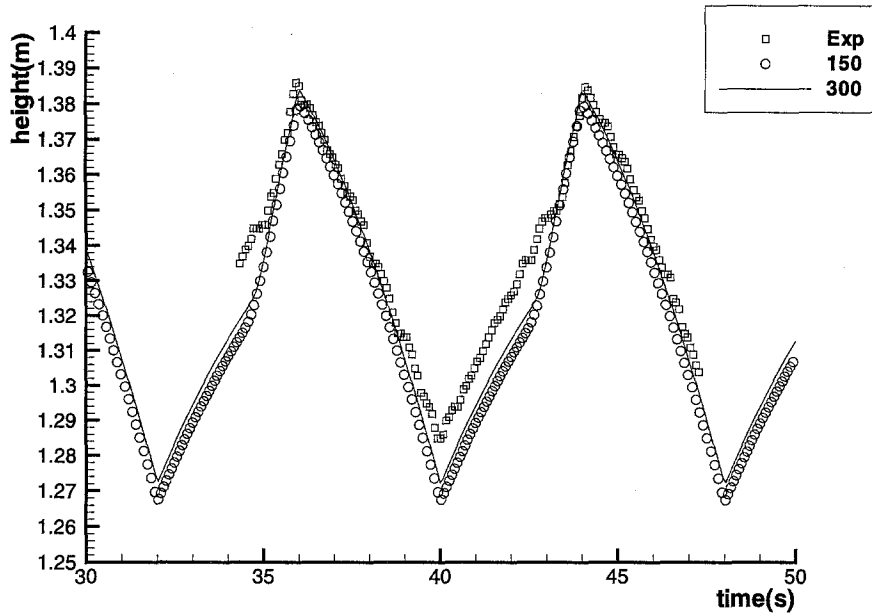
Figure 5. Case 1 with $C = 0$. Fifth-order WENO numerical method. Squares are the experimental data, circles are the simulation result with 150 grid points, and the solid line is the simulation result with 300 grid points.
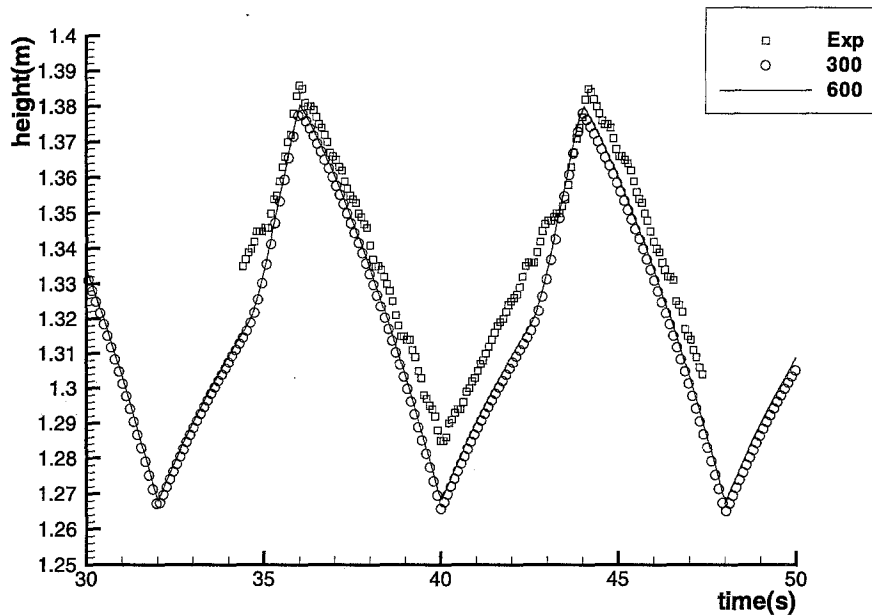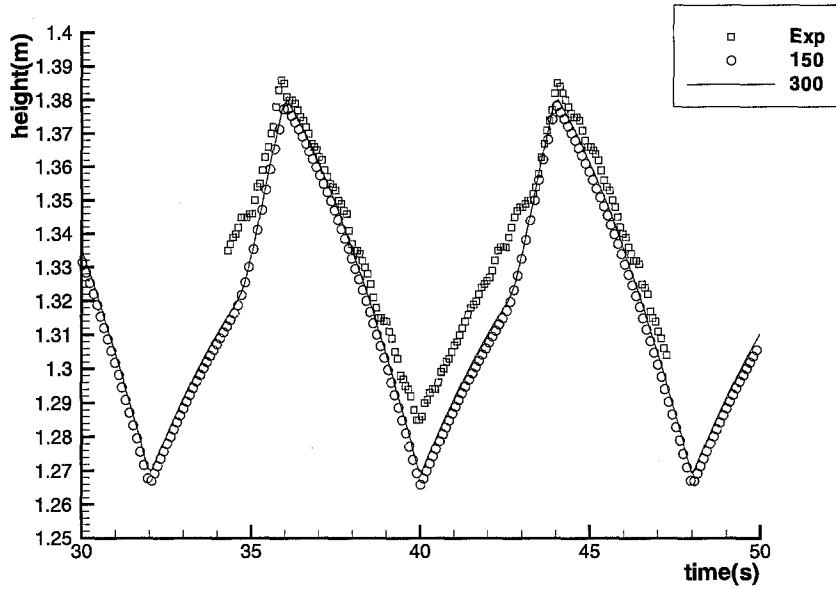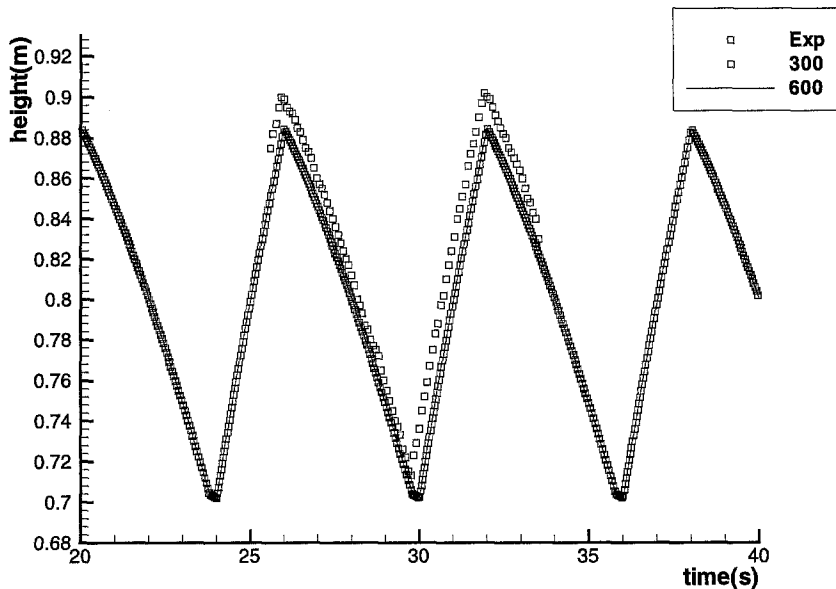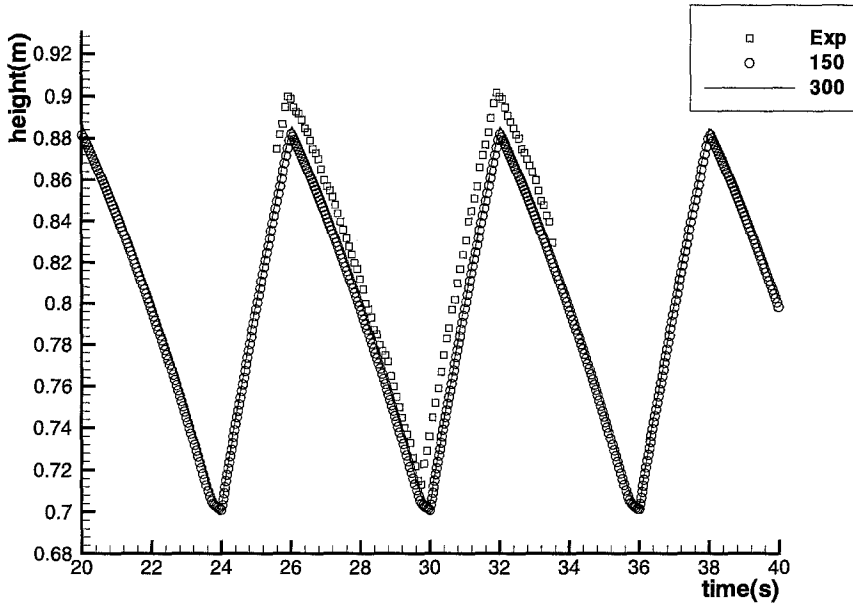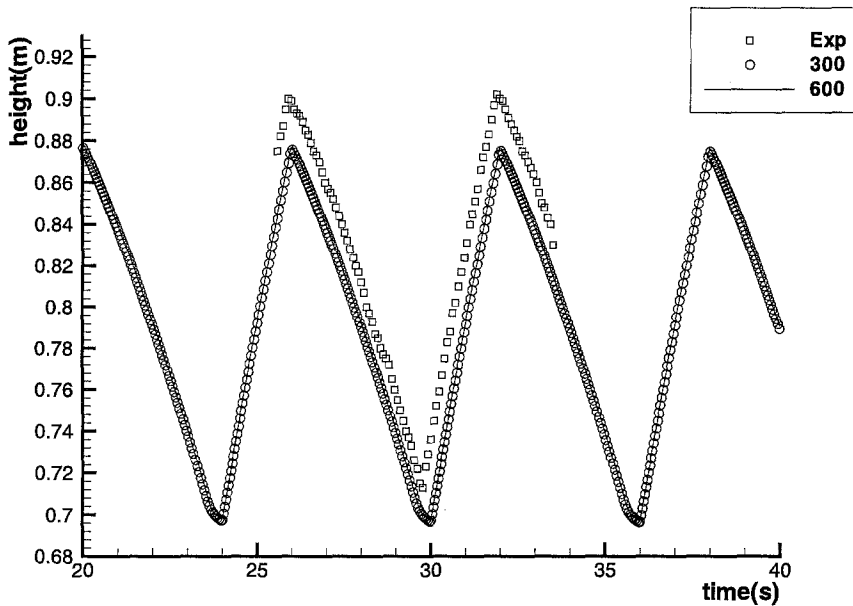

Figure 6. Case 1 with $C = 0.5$ and $\lambda = 3$. First-order numerical method. Squares are the experimental data, circles are the simulation result with 300 grid points, and the solid line is the simulation result with 600 grid points.

We summarize the numerical viscosity coefficients β_1 and β_2 in (3.6) and (3.7), and the co-efficient γ in front of the largest eigenvalue in (3.8) and (3.9), in Table 2. We have made sure to choose these values so that the numerical viscosity vanishes with grid refinement, justifying the term "numerical viscosity". Also notice that there is no numerical viscosity added for the second equation when $C = 0$ because the second equation comes from the momentum equations and actually contains physical viscosity. The results remain close when these parameters take values in a neighborhood of the chosen values. However, the bed height $h(t)$ does not stay in a
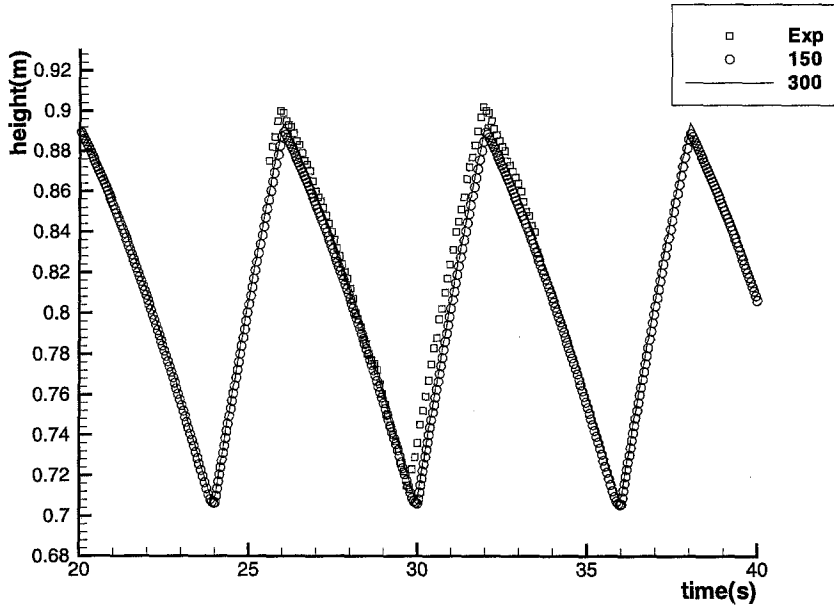
Figure 7. Case 1 with $C = 0.5$ and $\lambda = 3$. Fifth-order WENO numerical method. Squares are the experimental data, circles are the simulation result with 150 grid points, and the solid line is the simulation result with 300 grid points.

Figure 8. Case 2 with $C = 0$. First-order numerical method. Squares are the experimental data, circles are the simulation result with 300 grid points, and the solid line is the simulation result with 600 grid points.

time periodic fashion (rather it either increases or decreases without bound for large time) when these parameters are in the wrong range. It is not clear *a priori* mathematically that the bed height $h(t)$ to these models should maintain a periodic pattern in time with the given initial and boundary conditions.

Figures 4–7 are for the first case. Among them, Figure 4 represents the result for the model with $C = 0$ using the first-order method, and Figure 5 represents the result for the same model with $C = 0$ using the fifth-order WENO method. Figures 6 and 7 contain the first-order and fifth-order results, respectively, for the model with $C > 0$. We notice that convergence is observed
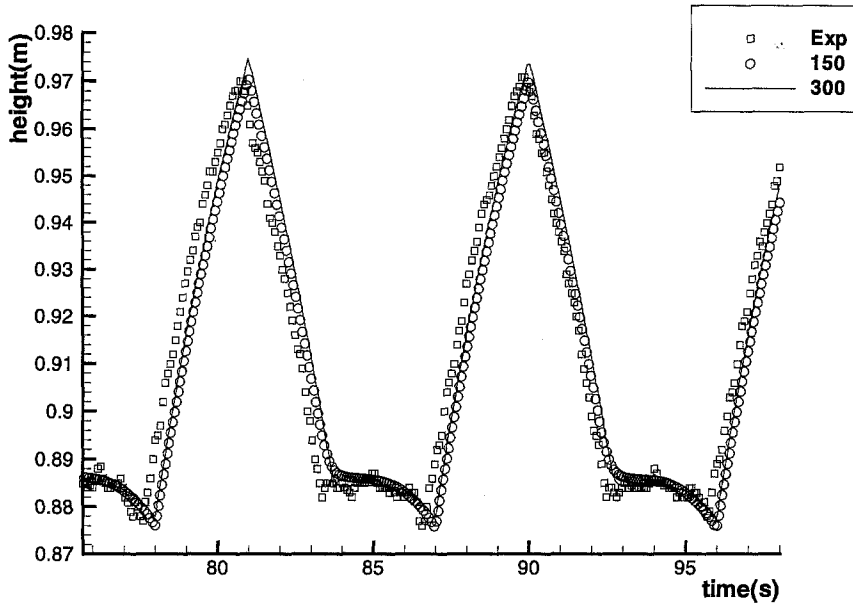
Figure 9. Case 2 with $C = 0$. Fifth-order WENO numerical method. Squares are the experimental data, circles are the simulation result with 150 grid points, and the solid line is the simulation result with 300 grid points.
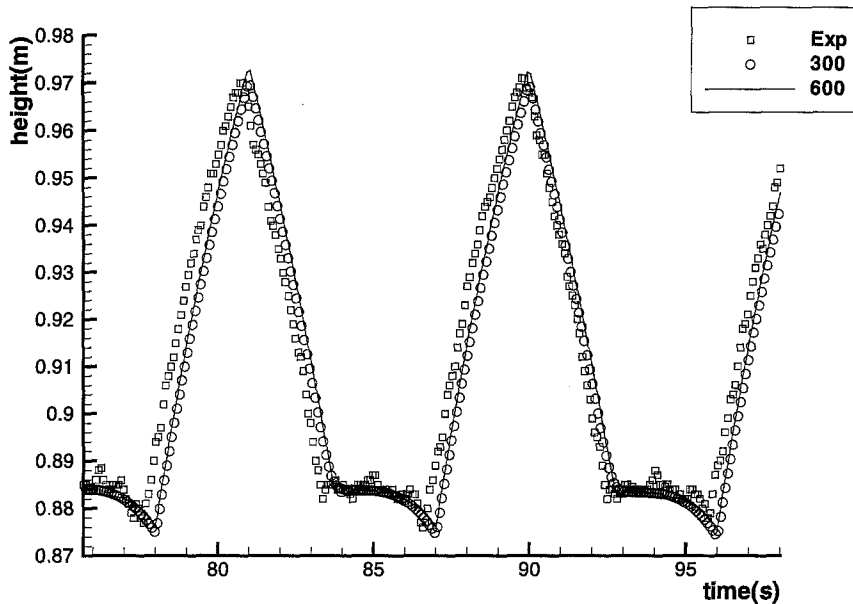

Figure 10. Case 2 with $C = 0.5$ and $\lambda = 3$. First-order numerical method. Squares are the experimental data, circles are the simulation result with 300 grid points, and the solid line is the simulation result with 600 grid points.

during mesh refinement for both numerical methods and both models. The numerical results are reasonably close to the experimental results for both models, however, the match seems to be better for the model with $C = 0$, especially for the first-order simulation result.

Figures 8–11 are for the second case. Among them, Figures 8 and 9 represent the results for the model with $C = 0$ using the first-order method and the fifth-order method, respectively. Figures 10 and 11 contain the first-order and fifth-order results, respectively, for the model with $C > 0$. Again, we notice that convergence is observed during mesh refinement for both numerical methods and both models. The numerical results are close to experimental data for both models.
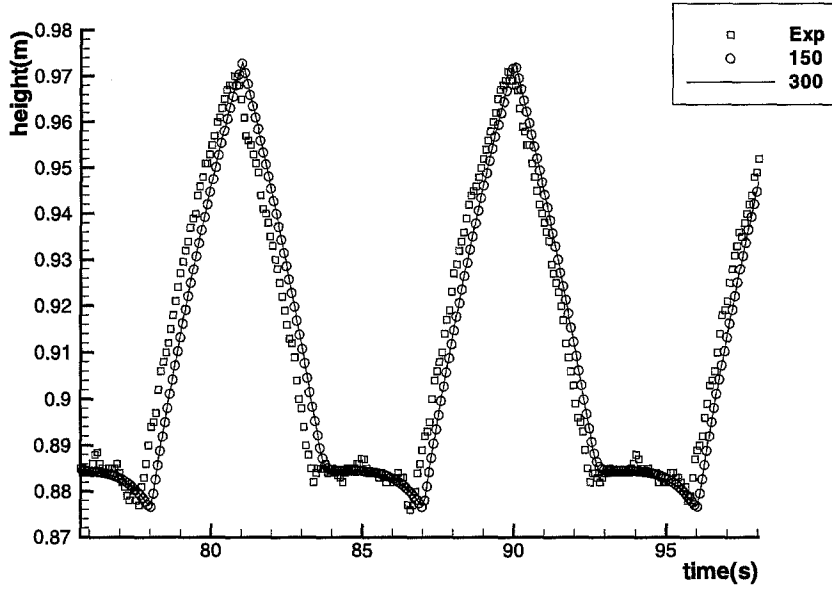
Figure 11. Case 2 with $C = 0.5$ and $\lambda = 3$. Fifth-order WENO numerical method. Squares are the experimental data, circles are the simulation result with 150 grid points, and the solid line is the simulation result with 300 grid points.
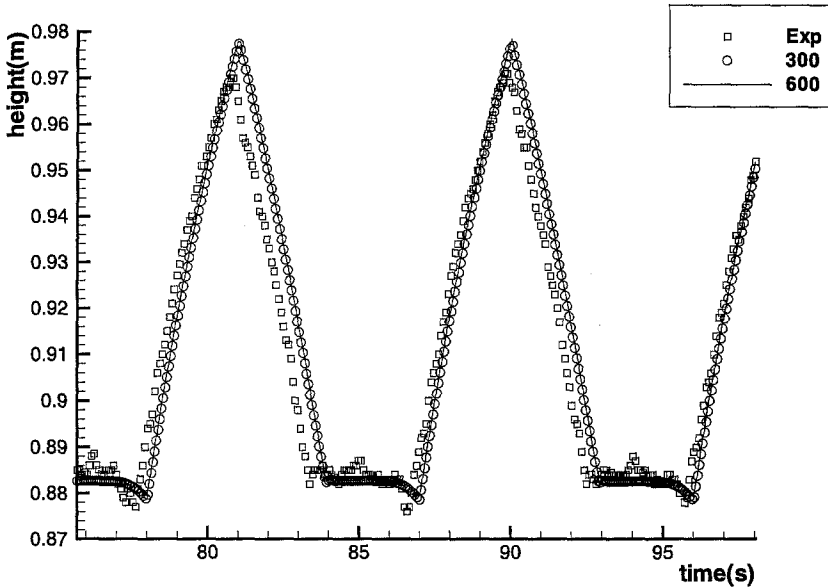
Figure 12. Case 3 with $C = 0$. First-order numerical method. Squares are the experimental data, circles are the simulation result with 300 grid points, and the solid line is the simulation result with 600 grid points.

It seems that the model with $C > 0$ fits the experimental result better for this case. It also seems that the fifth-order results are closer to the experimental results than the first-order results for this case, especially for the model with $C > 0$.

Figures 12–17 are for the third case. Among them, Figures 12 and 13 represent the results for the model with $C = 0$ using the first-order method and the fifth-order method, respectively. Figures 14 and 15 contain the first-order and fifth-order results, respectively, for the model with $C > 0$. Again, the numerical results are well converged for both methods and both models, and the agreement between the simulation results and experimental data is very good. Finally,

Figure 13. Case 3 with $C = 0$. Fifth-order WENO numerical method. Squares are the experimental data, circles are the simulation result with 150 grid points, and the solid line is the simulation result with 300 grid points.


Figure 14. Case 3 with $C = 0.5$ and $\lambda = 3$. First-order numerical method. Squares are the experimental data, circles are the simulation result with 300 grid points, and the solid line is the simulation result with 600 grid points.

Figures 16 and 17 contain the comparison between the simulation results and the experimental data for the volume fraction of particles α_p, for five equally spaced time snaps during a time period. Figure 16 is for the model with $C = 0$, and Figure 17 is for the model with $C > 0$. The first-order results are shown on the left, and the fifth-order results on the right. The solid lines represent the simulation results with the refined mesh, and the symbols are the experimental data. We can observe a reasonably good agreement between the simulation results and the experimental data for α_p. The results obtained by the fifth-order WENO method seem to be smoother (less numerical overshoot) near the junction than those obtained by the first-order method.

Figure 15. Case 3 with $C = 0.5$ and $\lambda = 3$. Fifth-order WENO numerical method. Squares are the experimental data, circles are the simulation result with 150 grid points, and the solid line is the simulation result with 300 grid points.

Table 2. Summary of the numerical viscosity coefficients.

Test Cases	Mesh	$C = 0$					$C = 0.5,$		$\lambda = 3$	
		First Order		Fifth Order			First Order		Fifth Order	
		β_1	β_2	β_1	β_2	γ	β_1	β_2	β_1	β_2
Case 1	Coarse	0.5	0	0.5	0	2.5	1.75	1.75	0.85	0.85
	Refined	0.5	0	0.5	0	4.0	3.0	3.0	1.2	1.2
Case 2	Coarse	0.75	0	0.5	0	0.15	2.0	2.0	0.448	0.448
	Refined	1.25	0	0.5	0	0.4	3.25	3.25	0.59	0.59
Case 3	Coarse	0.25	0	0.5	0	4.0	1.25	1.25	0.5	0.5
	Refined	0.375	0	0.5	0	5.0	1.5	1.5	0.9	0.9
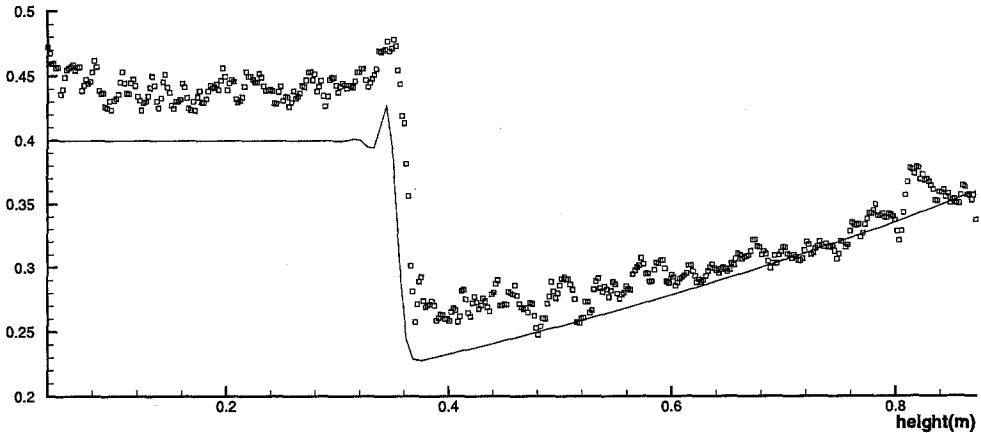
(a) Simulation results of the first-order method with 600 points at $t = 0.0$ in a period.

Figure 16. The α_p for Case 3 for the model with $C = 0$. Solid lines: simulation results; symbols: experimental data.
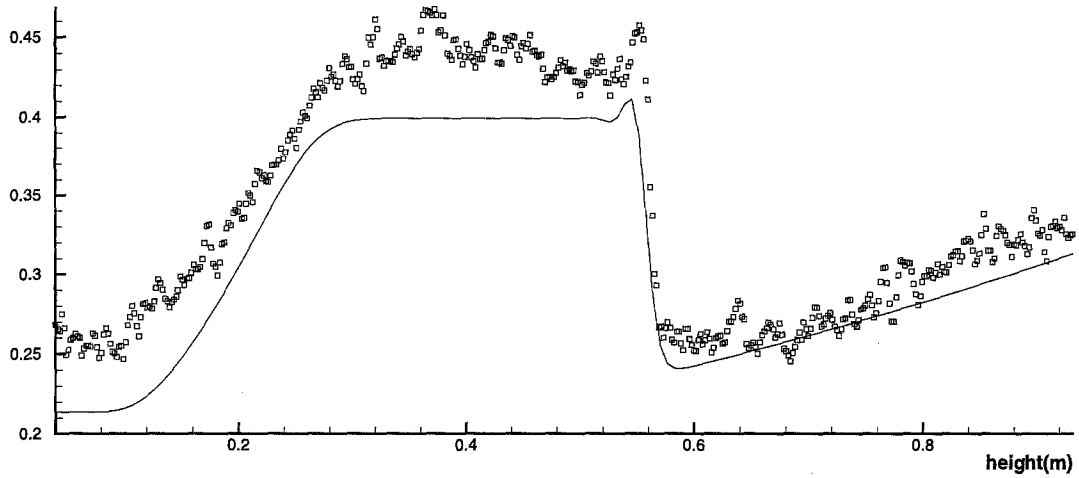
(b) Simulation results of the first-order method with 600 points at $t = 1.8$ in a period.
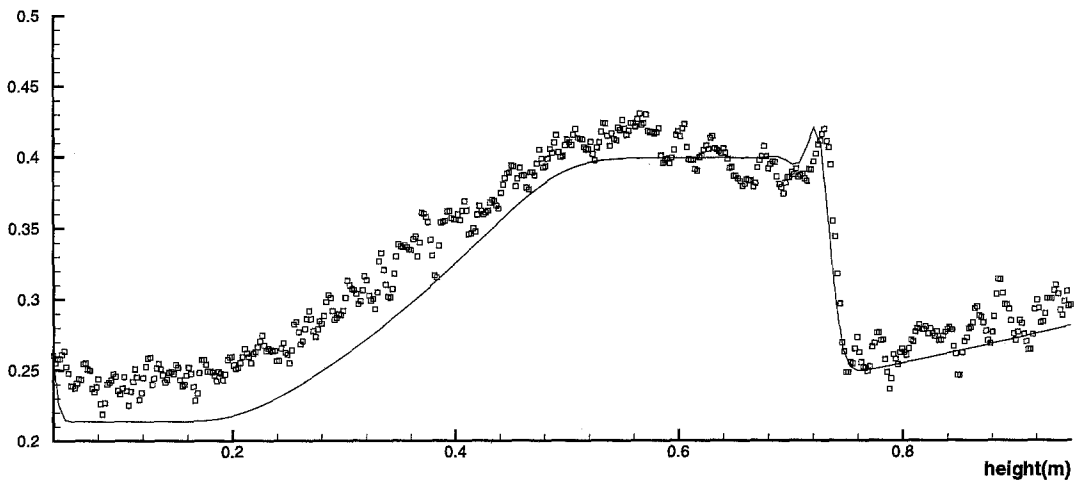
(c) Simulation results of the first-order method with 600 points at $t = 3.6$ in a period.
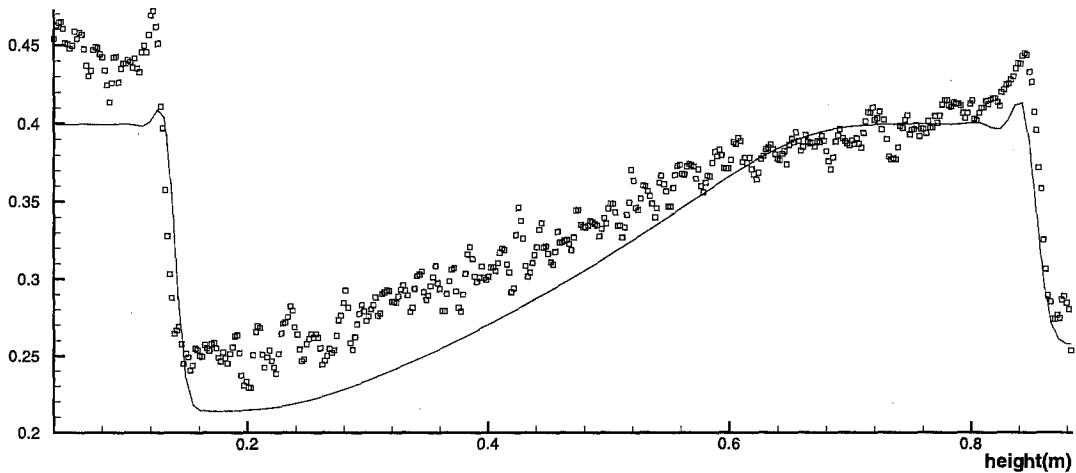
(d) Simulation results of the first-order method with 600 points at $t = 5.4$ in a period.
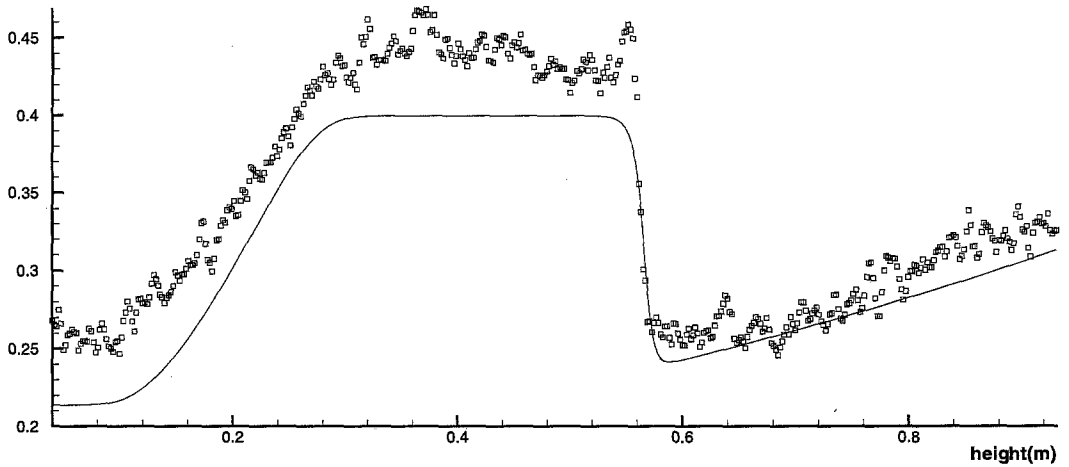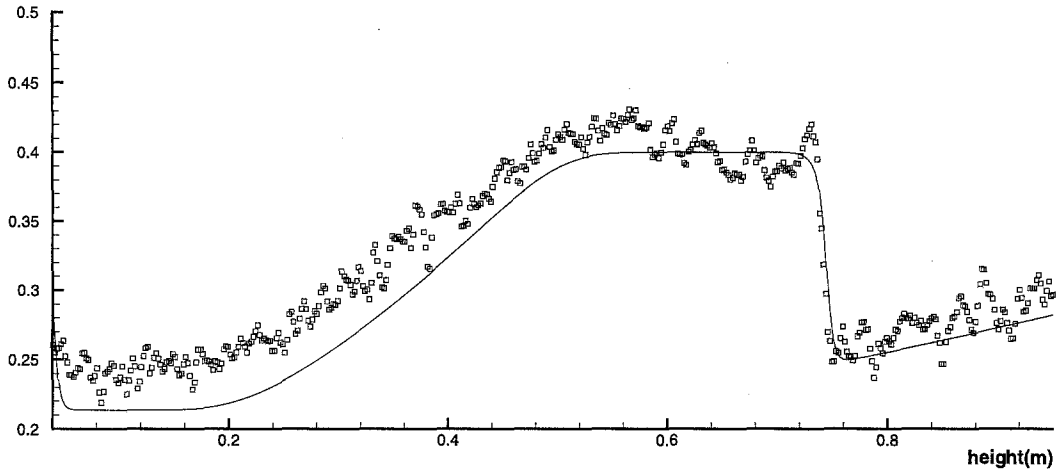
Figure 16. (cont.)
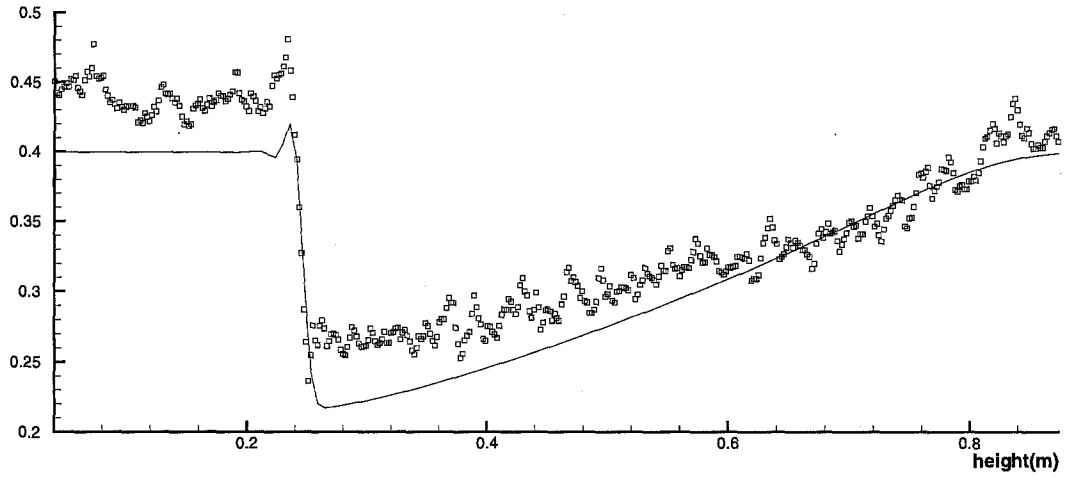
(e) Simulation results of the first-order method with 600 points at $t = 7.2$ in a period.
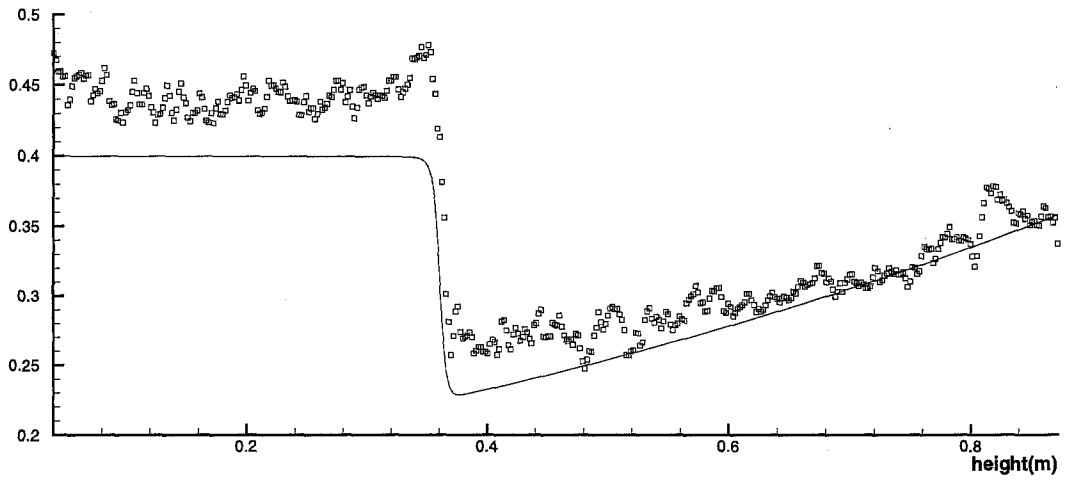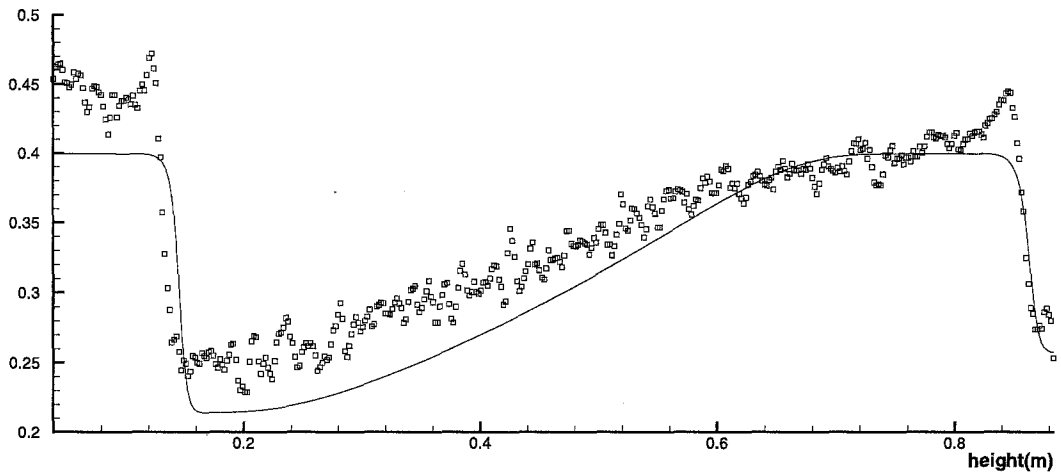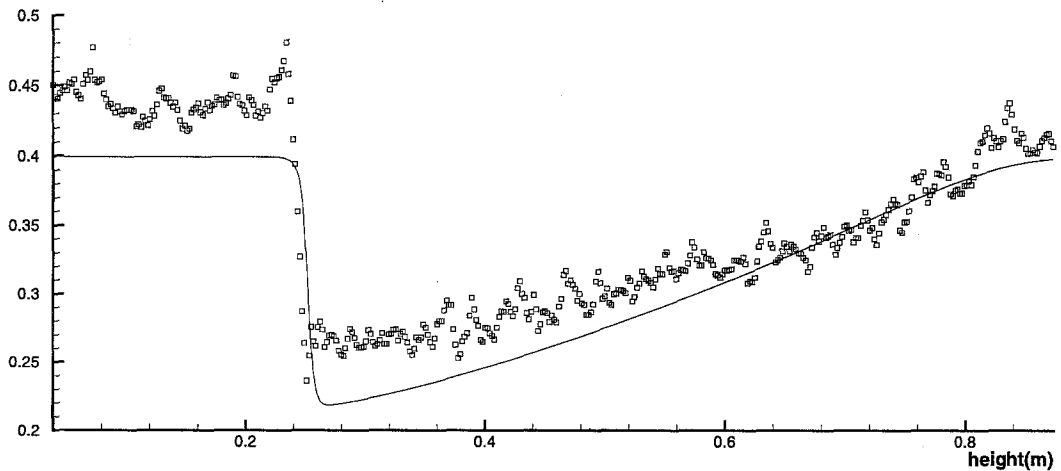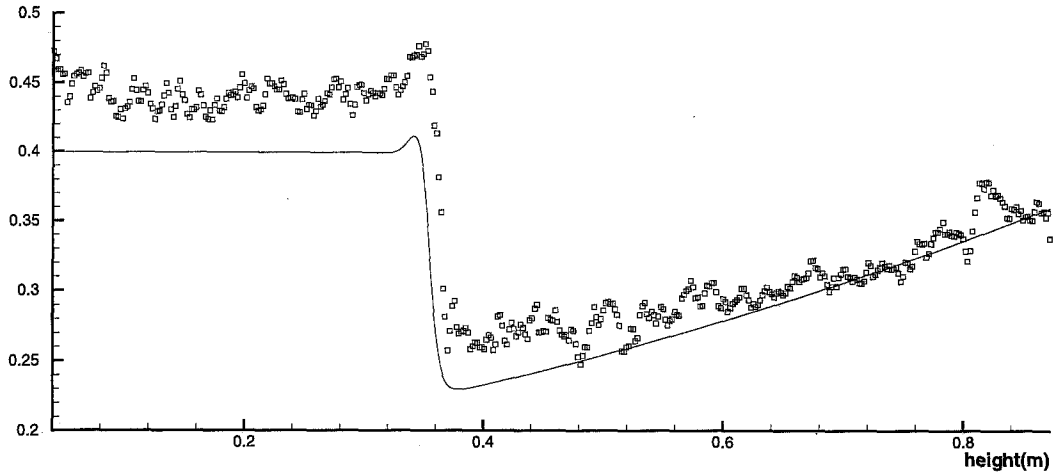

(f) Simulation results of the fifth-order WENO method with 300 points at $t = 0.0$ in a period.

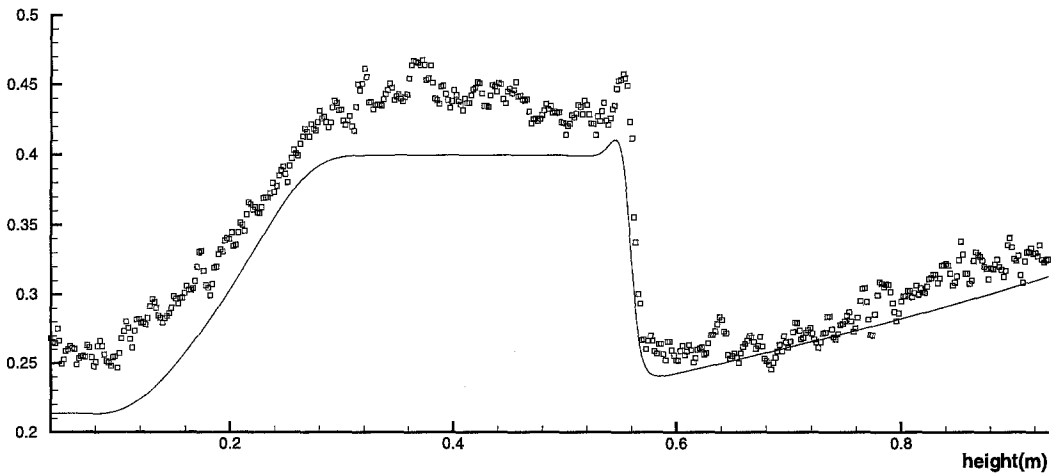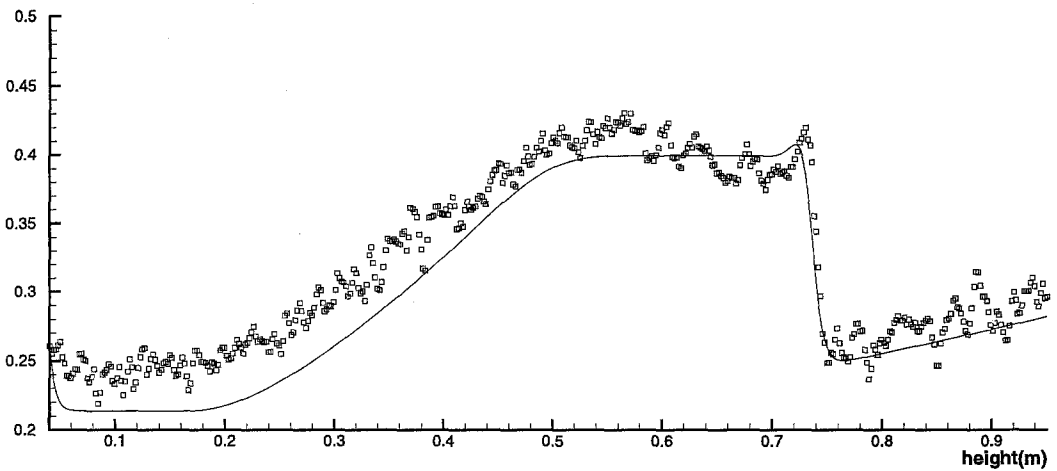(g) Simulation results of the fifth-order WENO method with 300 points at $t = 1.8$ in a period.

Figure 16. (cont.)

(h) Simulation results of the fifth-order WENO method with 300 points at $t = 3.6$ in a period.

(i) Simulation results of the fifth-order WENO method with 300 points at $t = 5.4$ in a period.

(j) Simulation results of the fifth-order WENO method with 300 points at $t = 7.2$ in a period.

Figure 16. (cont.)

(a) Simulation results of the first-order method with 600 points at $t = 0.0$ in a period.
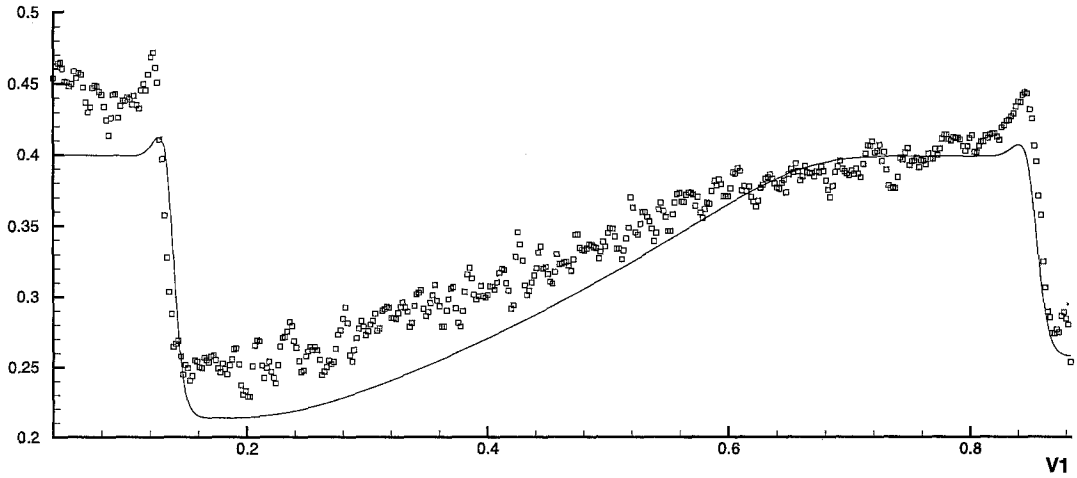

(b) Simulation results of the first-order method with 600 points at $t = 1.8$ in a period.
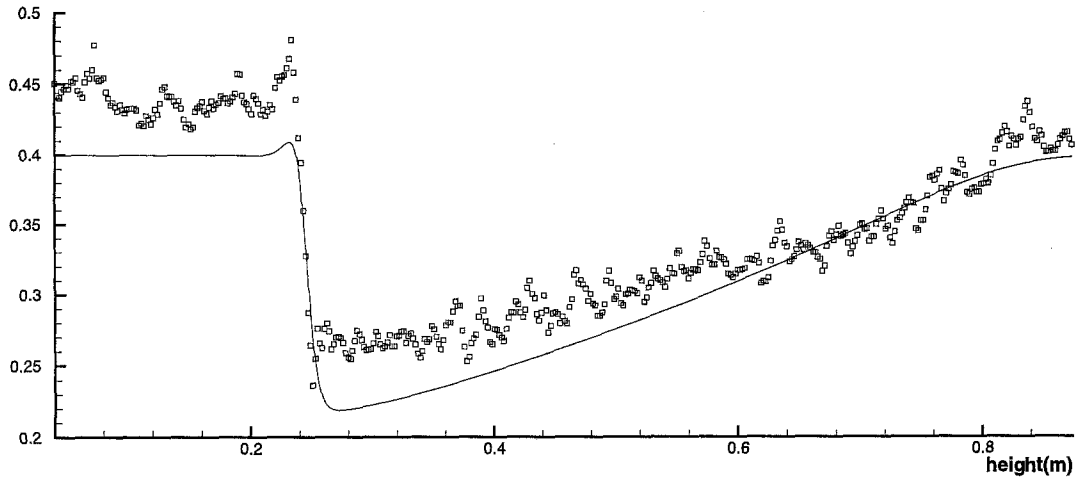

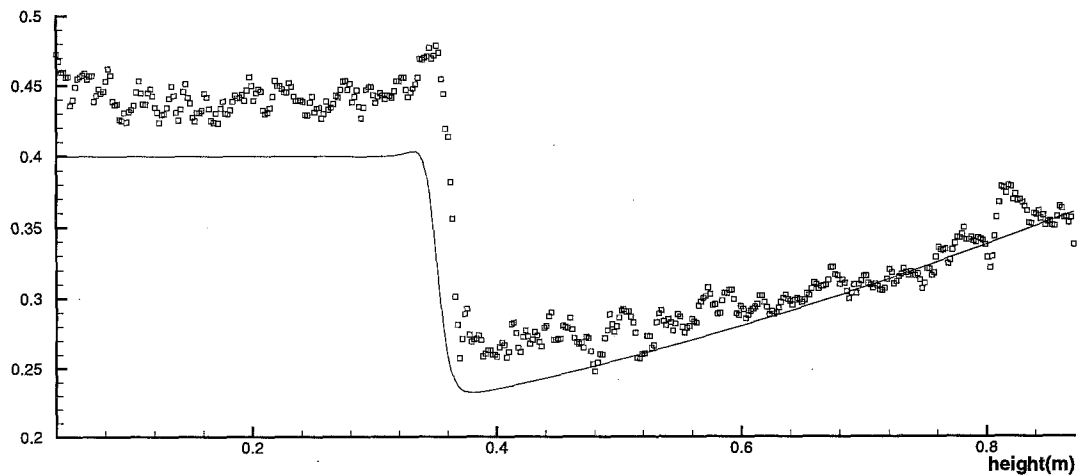(c) Simulation results of the first-order method with 600 points at $t = 3.6$ in a period.

Figure 17. The α_p for Case 3 for the model with $C = 0.5$ and $\lambda = 3$. Solid lines: simulation results; symbols: experimental data.

(d) Simulation results of the first-order method with 600 points at $t = 5.4$ in a period.
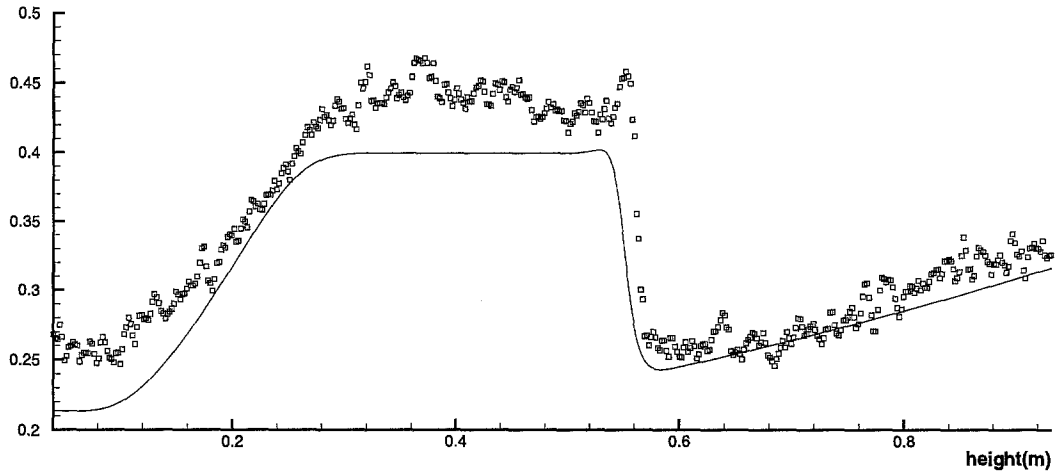

(e) Simulation results of the first-order method with 600 points at $t = 7.2$ in a period.
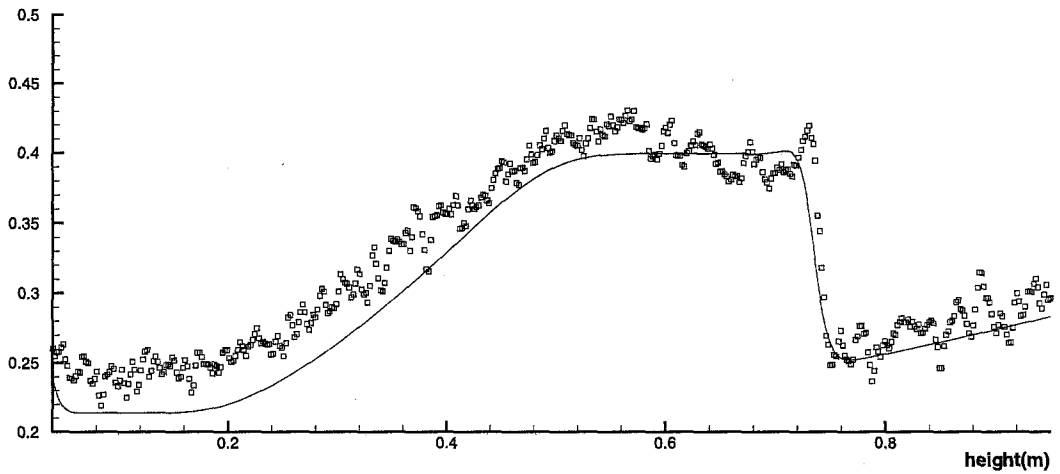

(f) Simulation results of the fifth-order WENO method with 300 points at $t = 0.0$ in a period.
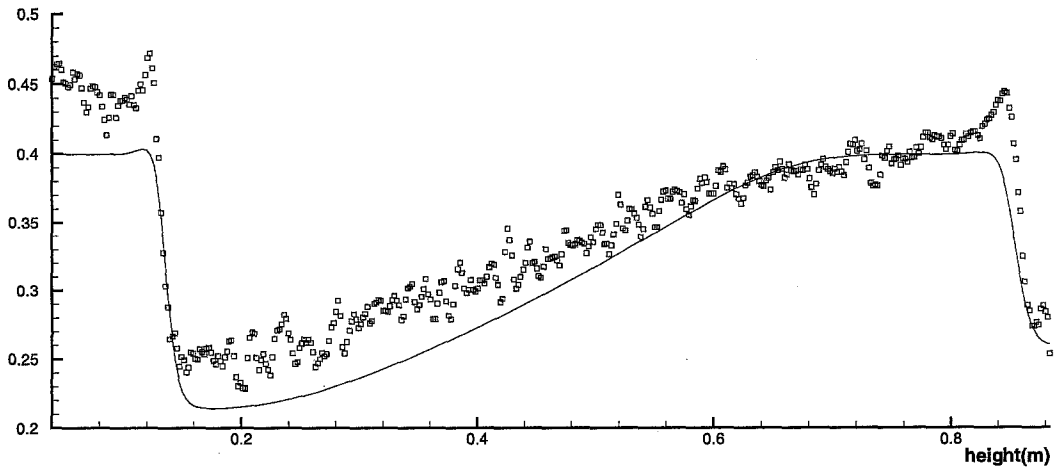
Figure 17. (cont.)

(g) Simulation results of the fifth-order WENO method with 300 points at $t = 1.8$ in a period.
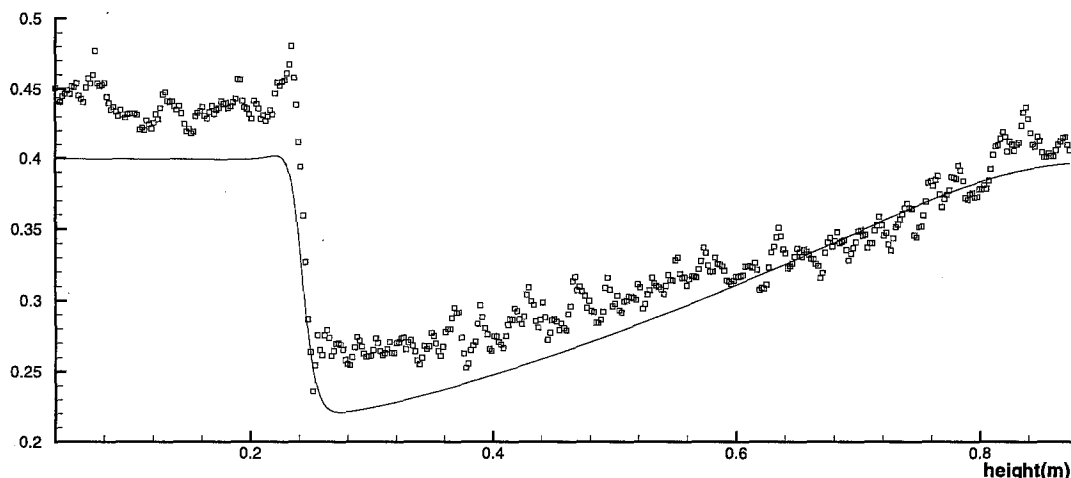

(h) Simulation results of the fifth-order WENO method with 300 points at $t = 3.6$ in a period.

(i) Simulation results of the fifth-order WENO method with 300 points at $t = 5.4$ in a period.

Figure 17. (cont.)

(j) Simulation results of the fifth-order WENO method with 300 points at $t = 7.2$ in a period.

Figure 17. (cont.)

6. CONCLUDING REMARKS

We have studied a general particle-fluid two-phase model involving a solid-liquid mixture medium. Two physical mechanisms to stabilize the system, one by additional physical viscosity and the other by additional virtual mass forces, are considered. Two different numerical methods, one first-order Lax-Friedrichs-type and the other fifth-order WENO scheme, are developed to solve this general system. A realistic pulsed liquid fluidized bed is simulated and the simulation results are compared with experimental data. It is found that both numerical methods converge well for all test cases during grid refinement, indicating their suitability for the simulation of such a general model. The fifth-order method provides better resolution for the same number of mesh points, or comparable resolution using fewer mesh points, when compared with the first-order method. Simulation results agree in general quite well with experimental data.

REFERENCES

1. G.-S. Jiang and C.-W. Shu, Efficient implementation of weighted ENO schemes, *Journal of Computational Physics* **126**, 202–228, (1996).
2. D. Balsara and C.-W. Shu, Monotonicity preserving weighted essentially non-oscillatory schemes with increasingly high order of accuracy, *Journal of Computational Physics* **160**, 405–452, (2000).
3. C.-W. Shu, A numerical method for systems of conservation laws of mixed type admitting hyperbolic flux splitting, *Journal of Computational Physics* **100**, 424–429, (1992).
4. C.-W. Shu, Essentially non-oscillatory and weighted essentially non-oscillatory schemes for hyperbolic conservation laws, In *Advanced Numerical Approximation of Nonlinear Hyperbolic Equations, Lecture Notes in Mathematics, Volume 1697*, (Edited by A. Quarteroni), pp. 325–432, Springer, (1998).
5. M.H.I. Baird, Vibrations and pulsations, *British Chemical Engineering* **11**, 20–25, (1966).
6. M. Kobayashi, D. Ramaswami and W.T. Brazelton, Pulsed-bed approach to fluidization, In *Chemical Engineering Progress Symposium Series—Fluidization Fundamentals and Application, Volume 66*, pp. 47–57, (1970).
7. D.V. Pence and D.E. Beasley, Local, instantaneous heat transfer in pulse-stabilized fluidization, In *Proceedings of the ASME Heat Transfer Division, Volume 334*, pp. 65–75, (1996).
8. W.H. Lee and R.W. Lyczkowski, The basic character of five two-phase flow model equation sets, *Int. J. Numer. Meth. Fluid* **33**, 1075–1098, (2000).
9. D. Gidaspow, *Multiphase Flow and Fluidization: Continuum and Kinetic Theory Descriptions*, Academic Press, (1994).
10. D. Gidaspow, Modeling of two-phase flow, In *Proceedings of the 5th International Heat Transfer Conference*, Tokyo, Japan, pp. 163–168, (1974).
11. R.W. Lyczkowski, Transient propagation behavior of two-phase flow equations, *Heat Transfer: Research and Application, AIChE Symp. Ser.* **75** (174), 165–174, (1978).
12. G. Rudinger and A. Chang, Analysis of non-steady two-phase flow, *Physics of Fluids* **7**, 1747–1754, (1964).

13. D. Drew, L. Cheng and R.T. Lahey, Jr., The analysis of virtual mass effects in two-phase flow, *International Journal of Multiphase Flow* **5**, 233–242, (1979).

14. R.T. Lahey, Jr., L. Cheng, D. Drew and J.E. Flaherty, The effect of virtual mass on the numerical stability of accelerating two-phase flows, *Int. J. Multiphase Flow* **6**, 281–294, (1980).

15. A.V. Jones and A. Prosperetti, On the suitability of the first-order differential models for two-phase flow prediction, *Int. J. Multiphase Flow* **11**, 133–148, (1985).

16. A. Prosperetti, Some considerations on the modeling of disperse multiphase flows by averaged equations, *JSME International Journal, Series B* **42**, 573–585, (1999).

17. D. Liu, *Fluid Dynamics of Two-Phase Systems* (in Chinese), Higher Education Press, Beijing, (1993).

18. S.C. Tsinontides and R. Jackson, The mechanics of gas fluidized beds with an interval of stable fluidization, *Journal of Fluid Mechanics* **255**, 237–274, (1993).

19. B.J. Glasser, I.G. Kevrekidis and S. Sundaresan, Fully developed travelling wave solutions and bubble formation in fluidized beds, *Journal of Fluid Mechanics* **334**, 157–188, (1997).

20. G.B. Wallis, *One-Dimensional Two-Phase Flow*, McGraw-Hill, New York, (1969).

21. G.K. Batchelor, A new theory of the instability of a uniform fluidized beds, *Journal of Fluid Mechanics* **193**, 75–110, (1988).

22. K.G. Anderson, S. Sundaresan and R. Jackson, Instabilities and the formation of bubbles in fluidized beds, *Journal of Fluid Mechanics* **303**, 327–366, (1995).

23. B.J. Glasser, I.G. Kevrekidis and S. Sundaresan, One- and two-dimensional travelling wave solutions in gas-fluidized beds, *Journal of Fluid Mechanics* **306**, 183–221, (1996).

24. G. Jin, Y. Nie and D. Liu, Numerical simulation of pulsed liquid fluidized bed and its experimental validation, *Powder Technology* **119**, 153–163, (2001).

25. C.-W. Shu and S. Osher, Efficient implementation of essentially non-oscillatory shock capturing schemes, *Journal of Computational Physics* **77**, 439–471, (1988).